

This is a preprint submitted to arXiv. The paper is currently under review.

A Vertically Resolved MSE Framework Highlights the Role of the Boundary Layer in Convective Self-Aggregation

Lin Yao¹, Da Yang^{*1,2}, and Zhe-Min Tan³

¹University of California, Davis, CA, USA.

²Lawrence Berkeley National Laboratory, Berkeley, CA, USA.

³Nanjing University, Nanjing, China

* *Corresponding author:* Da Yang, dayang@ucdavis.edu

Abstract

Convective self-aggregation refers to a phenomenon that random convection can self-organize into large-scale clusters over an ocean surface with uniform temperature in cloud-resolving models. Understanding its physics provides insights into the development of tropical cyclones and the Madden-Julian Oscillation. Here we present a vertically resolved moist static energy (VR-MSE) framework to study convective self-aggregation. We find that the development of self-aggregation is associated with an increase of MSE variance in the boundary layer (BL). We further show that radiation dominates the generation of MSE variance, which is further enhanced by atmospheric circulations. Surface fluxes, on the other side, consume MSE variance and then inhibits self-aggregation. These results support that the BL plays a key role in the development of self-aggregation, which agrees with recent numerical simulation results and the available potential energy analyses. Moreover, we find that the adiabatic production of MSE variance due to circulation mainly comes from the near-surface layer rather than the low-level circulation emphasized by previous literature. This new analysis framework complements the previous MSE framework that does not resolve the vertical dimension.

1. Introduction

Uniformly distributed convection can spontaneously cluster into large-scale upwelling areas over an ocean surface with uniform temperature in cloud-resolving model (CRM) simulations. This phenomenon is referred to as convective self-aggregation and has been extensively studied since Held et al. (1993) (Bretherton et al. 2005; Muller and Held 2012; Wing and Emanuel 2014; Emanuel et al. 2014; Muller and Bony 2015; Holloway and Woolnough 2016; Yang 2018a,b, 2019). Previous studies have suggested that tropical cyclones (Nolan et al. 2007; Boos et al. 2016) and the Madden-Julian Oscillation (MJO) (Arnold and Randall 2015) are special forms of convective self-aggregation on f -plane and β -plane, respectively. Therefore, investigating the underlying physics of self-aggregation can give additional insights into such tropical mysteries.

Previous studies have widely employed the moist static energy (MSE) to diagnose convectively coupled circulations in the tropical atmosphere (Neelin and Held 1987; Kiranmayi and Maloney 2011; Andersen and Kuang 2012; Arnold et al. 2013; Pritchard and Yang 2016). For example, Bretherton et al. (2005) predicted the initial e-folding rate of self-aggregation based on a vertically-integrated MSE (hereafter VI-MSE) budget. Following Andersen and Kuang (2012), Wing and Emanuel (2014) developed a budget equation for the VI-MSE variance [their Eq. (9)] and showed that the development of self-aggregation is associated with an increase in the VI-MSE variance. Based on this VI-MSE framework, the authors further attributed self-aggregation to individual physical processes, including radiative feedbacks, surface-flux feedbacks and circulation dynamics. The VI-MSE framework has then been extensively used

to study self-aggregation (Coppin and Bony 2015; Arnold and Randall 2015; Wing and Cronin 2016; Holloway and Woolnough 2016).

While the VI-MSE framework has provided many insights into the physics of self-aggregation, the vertical dimension remains too physically important to be integrated over (e.g., Mapes 2016). For example, recent studies have shown that the boundary layer (BL) is particularly important in convective self-aggregation (Jeevanjee and Romps 2013; Muller and Bony 2015; Naumann et al. 2017; Yang 2018a,b). Muller and Bony (2015) found that the radiative cooling profiles, especially the low-level cooling in dry patches, affect self-aggregation. Yang (2018b) showed that the development of self-aggregation is associated with increases in the available potential energy (APE)—the energy reservoir for self-aggregation circulations. The author then proposed and showed that physical processes in the BL dominate the APE production and are, therefore, key to convective self-aggregation. This “bottom-up” development of self-aggregation cannot be understood by using the VI-MSE framework, because it cannot resolve the vertical dimension.

Here we propose a vertically resolved MSE (hereafter VR-MSE) framework to study convective self-aggregation, which allows us to calculate the spatial MSE variance and its evolution at individual vertical levels. The VR-MSE framework complements that of the VI-MSE and can help test if the BL processes are key to the development of self-aggregation. In section 2, we will introduce the model setup. In section 3, we will first discuss the VI-MSE diagnostic framework and then propose a new VR-MSE analysis. In section 4, we will use the

VR-MSE framework to diagnose convective self-aggregation in a CRM simulation. We will also compare our results with the APE analysis in Yang (2018b). In Section 5, we will summarize the main findings and discuss the implications.

2. Numerical model setup

We use the System for Atmospheric Modeling (SAM, version 6.10.8) to simulate convective self-aggregation. SAM is an anelastic CRM (Khairoutdinov & Randall, 2003) and has been widely used to simulate self-aggregation (Bretherton et al. 2005; Muller and Held 2012; Khairoutdinov and Emanuel 2013; Wing and Emanuel 2014; Bretherton and Khairoutdinov 2015; Wing et al. 2016; Muller and Romps 2018; Yang 2018a,b, 2019). In this paper, we study a 2D (x-z) aggregation simulation over a horizontal periodic domain. The setup is identical to that of the control simulation in Yang (2018b) (his Figure 1a). The horizontal domain size is 2,048 km, and the horizontal resolution is 2 km. The model top is at 34.8 km. The vertical resolution is 50 m below 1 km and gradually increases to 600 m above 3 km. There is a 6-km sponge layer on the top of the model to damp out gravity wave reflection. The simulation runs for 150 days with a fixed uniform SST at 300K. The data is output hourly.

The radiative transfer scheme is the same as that of the National Center for Atmospheric Research Community Atmosphere Model (NCAR CAM3; Collins et al., 2006). The incident solar shortwave radiation is fixed at 413.9 W/m^2 to represent the climatological solar insolation received by the tropics. Considering that convective self-aggregation is a slow process, we turn off diurnal variations in the model for simplification. The microphysics is the

one-moment parameterization.

3. MSE theory

Following Yanai et al. (1973), the MSE (h) is defined as

$$h = c_p T + gz + L_v q_v \quad (1)$$

where c_p is the specific heat capacity at constant pressure, L_v is the latent heat of water vaporization, and q_v is the specific humidity of water vapor. Given that both the VI-MSE framework and the VR-MSE framework can be derived from the MSE budget, we start our analysis from the two-dimension MSE budget equation. Its flux form is given by

$$\partial_t h + \partial_x(uh) + \frac{1}{\rho_0} \partial_z(\rho_0 wh) = Q \quad (2)$$

where (u, w) are horizontal and vertical wind speeds, $\rho_0 = \rho_0(z)$ is the reference density, and $Q = Q_R + Q_F$ represents the MSE source due to radiation and surface fluxes, respectively. Here we assume that the MSE changes by sub-grid processes are negligible. We take the horizontal average of Eq. (2) and get

$$\overline{\partial_t h} + \overline{\partial_x(uh)} + \frac{1}{\rho_0} \overline{\partial_z(\rho_0 wh)} = \overline{Q} \quad (3)$$

The overbar donates the horizontal average, and $\overline{\partial_x(uh)} = 0$ because of the periodic domain.

Then we subtract Eq. (3) from Eq. (2), and get the MSE perturbations budget

$$\partial_t h' + \partial_x(uh) + \frac{1}{\rho_0} \partial_z(\rho_0 wh)' = Q' \quad (4)$$

Because we are only interested in perturbations associated with large-scale convective aggregation (denoted as \widetilde{A}' , A is a given variable), we apply both spatial (102-km) and temporal (5-day) running averages to filter out small-scale and high-frequency components.

The budget equation for the large-scale MSE perturbations (\widetilde{h}') is

$$\partial_t \widetilde{h}' + \partial_x(\widetilde{uh}) + \frac{1}{\rho_0} \partial_z(\widetilde{\rho_0 wh})' = \widetilde{Q}' \quad (5)$$

3.1 The VI-MSE framework

We first introduce a few useful definitions in the following analysis. The VI-MSE is defined as the total column MSE per unit area, which is

$$\hat{h} = \int_0^{z_t} \rho_0 h dz \quad (6)$$

where z_t is the height of the model top, and $\hat{A} = \int_0^{z_t} \rho_0 A dz$ denotes a density-weighted integral of variable A . The VI-MSE is closely linked to the column water vapor due to the weak temperature gradient (WTG) (Charney 1963; Sobel et al. 2001; Yang and Seidel 2020; Seidel and Yang 2020). Then the large-scale perturbations of \hat{h} related to self-aggregation is

$$\widehat{h}' = \int_0^{z_t} \rho_0 \widetilde{h}' dz \quad (7)$$

Hereafter, we denote the large-scale variable \widetilde{A} as A for simplification. Therefore, the corresponding VI-MSE variance (hereafter var_I) is

$$var_I = \overline{(\widehat{h}')^2} = \overline{\left(\int_0^{z_t} \rho_0 h' dz\right)^2} \quad (8)$$

Following Wing and Emanuel (2014), the budget equation for the VI-MSE variance [their Eq. (9)] can be derived from our Eq. (5) and (8). It is given by

$$\frac{1}{2} \partial_t (var_I) = \overline{\widehat{h}' \cdot SEF'} + \overline{\widehat{h}' \cdot RAD'} - \overline{\widehat{h}' \cdot (\partial_x \widehat{u} \widehat{h})} \quad (9)$$

where $SEF = \int_0^{z_t} \rho_0 Q_F dz$ is the surface enthalpy flux, $RAD = \int_0^{z_t} \rho_0 Q_R dz$ is the vertically integrated radiative cooling rate, and $\partial_x \widehat{u} \widehat{h}$ is the horizontal divergence of the VI-MSE flux. The vertical divergence $\frac{1}{\rho_0} \partial_z (\rho_0 w h)'$ vanishes after integral. The VI-MSE variance continually increases during convective self-aggregation, and the key of the framework is to evaluate processes generating var_I .

Here, we provide physical intuition for Eq. (9) in a two-layer atmosphere (Figure 1a). We assume that the thickness of each layer is H and is horizontally uniform. Then the VI-MSE variance (8) can be written as

$$var_I = \overline{\widehat{h}' \cdot \widehat{h}'} = \overline{(\rho_0 h'_1 H + \rho_0 h'_2 H)^2} = \rho_0^2 H^2 \left(\underbrace{\overline{h_1'^2 + h_2'^2}}_{\text{local variance}} + \underbrace{\overline{2h_1' h_2'}}_{\text{covariance}} \right) \quad (10)$$

where the subscripts of h' represent layer numbers. Eq. (10) contains two parts: the *local variance* within each layer and the *covariance* between the layers. The local variance represents the average intensity of energy perturbation, and larger values correspond to a more aggregated state. On the other hand, the covariance has little to do with the enhanced horizontal moisture variations and can be misleading. For example, if h'_1 and h'_2 are of large amplitudes but with the opposite signs, their covariance can be a large negative value. This can reduce var_I , which then represents a less aggregated state than reality. Therefore, it would be more precise to use the local variance instead of the whole VI-MSE variance as the diagnostic variable.

Similar ‘covariance’ components also exist in radiation and surface-flux terms in Eq. (9), which can be written as

$$\overline{\widehat{h}' \cdot RAD'} = \rho_0^2 H^2 \left(\underbrace{\overline{h'_1 Q_{R1}' + h'_2 Q_{R2}'}}_{\text{local forcing}} + \underbrace{\overline{h'_1 Q_{R2}' + h'_2 Q_{R1}'}}_{\text{remote forcing}} \right), \quad (11)$$

$$\overline{\widehat{h}' \cdot SEF'} = \rho_0 H \left(\underbrace{\overline{h'_1 SEF'}}_{\text{local forcing}} + \underbrace{\overline{h'_2 SEF'}}_{\text{remote forcing}} \right). \quad (12)$$

Equations (11) and (12) both contain two parts: the local forcing and the remote forcing. The local forcing is effective in modulating MSE variance directly: cooling low-MSE air at the same level further reduces the MSE. The remote forcing, however, lacks physical meanings. For

example, radiative cooling at $z = 10$ km only affects MSE anomalies at $z = 2$ km through generating subsidence. This is an indirect effect and is already accounted for by the advection or divergence term. This remote covariance is irrelevant to diagnose self-aggregation indeed.

We have illustrated the limitations of the VI-MSE framework using a two-layer atmosphere. Please see another demonstration using a CRM simulation in the Appendix. These analyses clearly call to develop a new MSE analysis framework that resolves the vertical dimension.

3.2 The VR-MSE framework

The VI-MSE variance was computed by first vertically integrating MSE anomalies and then calculating the spatial variance of the VI-MSE. However, the VR-MSE framework does the opposite: we first compute the spatial variance at each altitude and then perform the vertical integration, which is

$$var_R(z) = \frac{1}{2} \int_0^z \overline{(\rho_0 h')^2} dz', \quad (13)$$

Again, we simplify the large-scale variable \tilde{h}' to h' . This VR-MSE variance $var_R(z)$ represents the integrated MSE variance below an arbitrary height z . To get the budget equation for the VR-MSE variance, we multiply $\rho_0^2 h'$ on both sides of Eq. (5) and take a horizontal average on both sides, which is

$$\partial_t \frac{1}{2} \overline{(\rho_0 h')^2} = \rho_0^2 \overline{h' Q'} - \rho_0^2 h' \left[\frac{1}{\rho_0} \overline{\nabla(\rho_0 \vec{v} h)'} \right] \quad (14)$$

where $-\frac{1}{\rho_0}\nabla(\rho_0\vec{v}h)' = -[\partial_x(uh) + \frac{1}{\rho_0}\partial_z(\rho_0wh)']$ is the sum of horizontal and vertical convergence of MSE flux anomalies, representing the adiabatic production of h' (Eq. (5)). Hereafter, we refer to $-\frac{1}{\rho_0}\nabla(\rho_0\vec{v}h)'$ as MSE advection and denote it as $A_{h'}$. Eq. (14) is the *local* MSE variance budget, where diabatic heating/cooling can only change MSE anomalies locally. For example, the radiative cooling rate Q_{R_1}' can only change MSE anomalies in the same layer h_1' in the two-layer model (Figure 1a). Then we integrate (14) in z direction:

$$\partial_t \frac{1}{2} \int_0^z \overline{(\rho_0 h')^2} dz' = \int_0^z \overline{\rho_0^2 h' Q'} dz' - \int_0^z \overline{\rho_0^2 h' \left[\frac{1}{\rho_0} \nabla(\rho_0 \vec{v} h)' \right]} dz' \quad (15)$$

Eq. (15) is the VR-MSE variance budget. Finally, we normalize (15) with a column VR-MSE variance ($var_R(z_t) = \frac{1}{2} \int_0^{z_t} \overline{(\rho_0 h')^2} dz'$) to illustrate more details in the initial stage:

$$\underbrace{\frac{\partial_t \frac{1}{2} \int_0^z \overline{(\rho_0 h')^2} dz'}{var_R(z_t)}}_{\text{growth rate}} = \underbrace{\frac{\int_0^z \overline{\rho_0^2 h' Q'} dz'}{var_R(z_t)}}_{\text{diabatic production}} - \underbrace{\frac{\int_0^z \overline{\rho_0^2 h' \left[\frac{1}{\rho_0} \nabla(\rho_0 \vec{v} h)' \right]} dz'}{var_R(z_t)}}_{\text{adiabatic production}}. \quad (16)$$

Eq. (16) is the normalized VR-MSE variance budget, the key equation in our framework. The left-hand-side term is the growth rate of the VR-MSE variance, and the right-hand-side terms represent the diabatic and adiabatic productions of VR-MSE variance. Diabatic processes including radiation and surface fluxes can produce/consume the VR-MSE variance by coupling with the MSE anomalies. For example, anomalous radiative cooling/heating in drier/moister areas will promote convective self-aggregation by increasing the VR-MSE variance. Meanwhile, large-scale circulations can redistribute the MSE adiabatically, generating MSE

variance. In the following analysis, we will compute the advection term as the residual of Eq. (5), as done by Bretherton et al. (2005) and Wing and Emanuel (2014).

This VR-MSE framework is different from the VI-MSE framework because it focuses on the increase of MSE variance at individual layers. Therefore, the diabatic processes can only change the MSE variance locally, and their remote effects are achieved by circulations. Additionally, the budget equation of the VR-MSE variance can illustrate the vertical structure of convective self-aggregation, which cannot be achieved by the VI-MSE framework.

4. Results

We use Eq. (14) and (16) to diagnose convective self-aggregation in the control simulation. We will show its evolution and vertical structure and will illustrate the importance of the BL.

Figure 1b plots the precipitable water (PW, mm) in the control simulation. Based on the PW evolution, we divide the simulation into three stages: initialization (first 25 days), development (day 25-80) and equilibrium (day 80-150). An expanding dry patch centered at $x = 700$ km starts to form around day 25. Another dry hole emerges ten days later at $x = 1500$ km. After day 80, the whole system reaches its statistical equilibrium, and there are two convective aggregates with a spatial scale of about 1000 km. This spatial scale is consistent with simulation results presented by Yang (2018a), who also provided a quantitative explanation for what sets the size of convective aggregates.

The VR-MSE variance describes the evolution of self-aggregation. Figure 2a illustrates the evolution of variances of the VR-MSE and the PW. The column VR-MSE variance increases together with the PW variance before day 80, and then they both oscillate around a reference value. This is consistent with Figure 1b, suggesting that the development of aggregation is associated with increases in VR-MSE variance. Figure 2a further shows that the column VR-MSE variance is dominated by that in the lowest 2 km (dashed line), suggesting a bottom-heavy vertical structure. This is confirmed by the vertical structure of the MSE variance ($\overline{(h')^2}$). Figure 2b shows that much of the MSE variance is within the lowest 2 km of the atmosphere and that the MSE variance is dominated by the moisture variance ($\overline{(L_v q')^2}$, Figure 2c). This bottom-heavy structure is likely because the water vapor mixing ratio exponentially decreases in altitude with a scale height of about 2 km. This result supports the hypothesis that physical processes in the BL are key to the development and maintenance of convective self-aggregation (Yang 2018b).

Figure 2d plots the normalized VR-MSE variance budget [see Eq. (16)] and shows the importance of the BL. The green line represents the net growth rate of self-aggregation, which describes the temporal evolution of the VR-MSE variance. A positive value suggests an overall tendency to aggregate. The dark blue line denotes variance production by radiation, and the light blue one denotes that by surface fluxes. Positive values suggest that the corresponding diabatic process increases VR-MSE variance and promotes aggregation. The yellow line measures the contribution of the adiabatic production of MSE variance. A positive value indicates upgradient MSE transport, favoring aggregation. Solid lines correspond to column

integrals in Eq. (16) ($z = z_t$), while dashed lines correspond to the BL integrals ($z = 2 \text{ km}$). Their differences measure the contribution of the free troposphere (FT). Initially, the VR-MSE variance increases rapidly in both BL and FT. After a dry patch forms (around day 25), the BL starts to dominate the production of MSE variance, increasing MSE variance locally. This result is consistent with the VR-MSE variance plots in Figure 2a&b.

Figure 2d also supports the notion that dominant mechanisms in generating MSE variance might be distinct in different stages of convective self-aggregation (Wing and Emanuel 2014). In the initial stage, radiative feedbacks and atmospheric circulations make a positive contribution to convective self-aggregation. In the development stage, however, the production of MSE variance by radiation becomes bottom-heavy and is nearly balanced by the negative contribution due to surface fluxes. At this stage, the net diabatic production of MSE variance is close to zero or even negative. Meanwhile, adiabatic production is also bottom-heavy and is responsible for the development of self-aggregation.

Figure 3 explicitly shows the evolution of *local* MSE variance in time and altitude. The left column illustrates the results of the variance budget [see Eq. (14)], and the right two columns illustrate the evolution of MSE anomalies, radiative cooling rate anomaly and MSE advection in two time periods: day 10-20 (middle) and day 50-60 (right). The first period is in the initiation phase, and the second period is in the development phase. Figure 3a plots the *local* tendency of VR-MSE variance ($\partial_t \frac{1}{2} \overline{(\rho_0 h')^2}$), measuring how fast self-aggregation evolves at a given altitude. We observe a bottom-heavy structure: the MSE tendency is primarily in the BL, the

lowest 2 km of the atmosphere. During the initiation phase, moisture starts to organize, and dry holes form in the lower FT (Figure 3b). MSE anomalies in the BL is weak. During the developing phase, the MSE anomalies are significantly intensified in the BL (Figure 3c), consistent with the bottom-heavy tendency term. However, the FT MSE anomalies do not change much because the moisture variance is dominated by the BL (Figure 2c), and that the FT temperature anomalies are small due to the WTG (Charney 1963; Sobel et al. 2001; Yang and Seidel 2020; Seidel and Yang 2020). Figure 3a-c suggests that even though the MSE anomalies in the lower FT are considerable initially, the BL is responsible for increasing MSE variance and the development of convective self-aggregation.

Figure 3d shows the production of local MSE variance by radiative cooling. Positive values suggest that radiative feedback increases the MSE variance, leading to self-aggregation. Again, the radiative MSE variance production has a bottom-heavy structure. Most production is within the lowest 2 km, which highlights the importance of BL. In the initial stage, the MSE and radiative cooling anomalies are positively correlated in the FT, increasing MSE variance and promoting self-aggregation (Figure 3e). But they are negatively correlated in the BL, decreasing MSE variance and inhibiting aggregation locally. Since MSE anomalies are weak in the BL, the overall radiative effect is positive, promoting self-aggregation in the first 20 days (Figure 2d). In the development stage, the MSE and radiative cooling anomalies become positively correlated in the entire troposphere, and their amplitudes increase considerably in the BL, especially in the dry regions (Figure 3f). Therefore, the BL radiative process, especially clear-sky radiation, is primarily responsible for self-aggregation after the dry hole reaches to the BL.

Figure 3g measures the adiabatic production of MSE variance by large-scale circulations. Here we exclude the near-surface contribution due to its large magnitude, which will be discussed in Figure 4. In Figure 3, the advection is the major process to balance the variance production by radiative cooling. It has a similar bottom-heavy structure. Negative values represent that the downgradient advection reduces MSE variance and inhibits self-aggregation. Figure 3h-i show MSE advection $A_h' (-\frac{1}{\rho_0} \nabla(\rho_0 \vec{v}h)')$. Positive values denote local convergence of MSE anomalies (accumulation of MSE) while the negative denotes the divergence (consumption of MSE). Initially (Figure 3h), MSE anomalies and its advection are out of phase in the FT and in phase in the BL, which is likely due to the low-level circulation (Bretherton et al. 2005; Muller and Held 2012; Jeevanjee and Romps 2013; Coppin and Bony 2015). In the developing stage, their anomalies are enhanced and become negatively correlated, reducing MSE variance (Figure 3i). Generally, the advection above the near-surface layer is dominated by the BL and inhibits convective self-aggregation (Figure 3g).

Figure 4 gives more details on surface fluxes and near-surface advection. The heating rate by surface fluxes Q_{F_s}' (Figure 4a) has the opposite phase with the near-surface MSE anomalies h_s' (Figure 4c), so surface fluxes reduce MSE variance and inhibit convective self-aggregation (Figure 2d). Note that the magnitude of Q_{F_s}' is two orders of magnitude larger than that of Q_R' at the near-surface layer (Figure 3f). This is because surface-flux heating should balance the vertically integrated radiative cooling at steady state, which is

$$SEF' = -RAD' = -\int_0^{z_t} \rho_0 Q_R' dz \quad (17)$$

Remember, $SEF' = \int_0^{z_t} \rho_0 Q_F' dz$, and Q_F' only has values at the near-surface level, so the magnitude of Q_{F_s}' is much larger than that of Q_R' . Meanwhile, because the radiative cooling rate cannot change much locally, near-surface advection itself A_{h_s}' has to be large enough to balance the considerable Q_{F_s}' at the steady stage. In Figure 4b, large near-surface advection has the same phase with near-surface MSE anomalies. It increases near-surface MSE variance and promotes self-aggregation.

Figure 4d further shows normalized advection terms integrated over different vertical layers. Consistent with Figure 4b, near-surface advection promotes self-aggregation during the whole simulation except for initial adjustments. Deep advection (advection above 2 km) is generally the sink of MSE variance, and shallow advection (advection in the BL above the near-surface level) increases MSE variance in the initial stage. However, shallow advection inhibits aggregation after day 25, even though there is upgradient transport of MSE anomalies by the low-level circulation. In summary, near-surface advection has such a strong positive effect that it dominates over the negative contributions due to advection in the above layers (Figure 4). Therefore, even though the shallow and deep advection are generally negative (Figure 3g), the overall effect of advection is to promote convective self-aggregation by adiabatically generating MSE variance (Figure 2d).

5 Conclusion and Discussion

In this paper, we first show the limitations of the vertically integrated MSE (VI-MSE) framework to study the development of convective self-aggregation. Previous studies have extensively calculated a VI-MSE variance budget to diagnose the roles of different processes in aggregation. However, we find that the VI-MSE variance contains a covariance component between MSE anomalies at different altitudes [Eq. (10)], and that the VI-MSE variance production also includes such covariance [Eq. (11)-(12)]. Such covariance does not contribute to changes in local MSE variance and thus convective self-aggregation. Additionally, the VI-MSE framework does not have vertical resolutions and cannot show which layer is the key to convective self-aggregation. These limitations call for a new framework.

Here we present a vertically resolved MSE (VR-MSE) framework that focuses on changes of the local MSE variance [Eq. (14)]. We first show that the local MSE variance has a bottom-heavy structure, which is likely due to the exponential decrease of water vapor with altitude (Figure 2a-c). We further show that both diabatic and adiabatic productions of MSE variance share a similar bottom-heavy structure, leading to the primary increase of MSE variance in the BL. Our results are consistent with the previous APE analysis and mechanism-denial experiments and support the hypothesis that physical processes in the BL are key to self-aggregation (Yang 2018b; Muller and Bony 2015; Naumann et al. 2017).

We find adiabatic processes favor self-aggregation in the development stage (yellow line in Figure 2d). It seems consistent with previous studies, which proposed that the upgradient MSE transport by the low-level circulation favors self-aggregation (Bretherton 2005; Muller and

Bony 2015). However, here we demonstrate that the adiabatic MSE production is mainly in the near-surface layer (Figure 4d). This is because near-surface advection needs to be large enough to balance the considerable contribution from surface fluxes, which cannot be achieved by local radiative cooling. It implies that the low-level circulation may not be that important for self-aggregation. This is a unique result of the VR-MSE framework, which explicitly resolves the vertical dimension.

We can further apply the VR-MSE framework to study other convectively coupled circulations, such as the MJO. Previous studies have been widely using the VI-MSE framework to investigate the evolution of the MJO, even though the framework cannot resolve the vertical structure (Andersen and Kuang 2012; Arnold and Randall 2015; Pritchard and Yang 2016; Kiranmayi and Maloney 2011; Maloney 2009; Sobel et al. 2014). However, Wolding and Maloney (2015) proposed that the radiative cooling profile is essential to the moistening and drying of the lower and middle troposphere associated with the MJO. Therefore, resolving the vertical dimension might be crucial to understand the development and propagation of the MJO.

Acknowledgment:

This work was supported by the Laboratory Directed Research and Development (LDRD) funding from Berkeley Lab, provided by the Director, Office of Science, of the U.S. Department of Energy under Contract DE-AC02-05CH11231, by the U.S. Department of Energy, Office of Science, Office of Biological and Environmental Research, Climate and Environmental Sciences Division, Regional & Global Climate Modeling Program, under Award DE-AC02-05CH11231, and by the Packard Fellowship for Science and Engineering (to D.Y.).

APPENDIX

Matrices of the VI-MSE budget using CRM results

We show the VI-MSE variance and its production due to radiative cooling using the CRM results in the control simulation (Figure A1). The off-diagonal components represent the covariance across different vertical layers and are not directly relevant to the development of self-aggregation.

REFERENCES

- Andersen, J. A., and Z. Kuang, 2012: Moist static energy budget of MJO-like disturbances in the atmosphere of a zonally symmetric aquaplanet. *J. Clim.*, **25**, 2782–2804, <https://doi.org/10.1175/JCLI-D-11-00168.1>.
- Arnold, N. P., and D. A. Randall, 2015: Global-scale convective aggregation: Implications for the Madden-Julian Oscillation. *J. Adv. Model. Earth Syst.*, **7**, 1499–1518, <https://doi.org/10.1002/2015MS000498>.
- , Z. Kuang, and E. Tziperman, 2013: Enhanced MJO-like variability at high SST. *J. Clim.*, **26**, 988–1001, <https://doi.org/10.1175/JCLI-D-12-00272.1>.
- Boos, W. R., A. Fedorov, and L. Muir, 2016: Convective self-aggregation and tropical cyclogenesis under the hypohydrostatic rescaling. *J. Atmos. Sci.*, **73**, 525–544, <https://doi.org/10.1175/JAS-D-15-0049.1>.
- Bretherton, C. S., and M. F. Khairoutdinov, 2015: Convective self-aggregation feedbacks in near-global cloud-resolving simulations of an aquaplanet. *J. Adv. Model. Earth Syst.*, **7**, 1765–1787, <https://doi.org/10.1002/2015MS000499>.
- , P. N. Blossey, and M. Khairoutdinov, 2005: An energy-balance analysis of deep convective self-aggregation above uniform SST. *J. Atmos. Sci.*, **62**, 4273–4292, <https://doi.org/10.1175/JAS3614.1>.
- Charney, J. G., 1963: A Note on Large-Scale Motions in the Tropics. *J. Atmos. Sci.*, **20**, 607–609, [https://doi.org/10.1175/1520-0469\(1963\)020<0607:anolsm>2.0.co;2](https://doi.org/10.1175/1520-0469(1963)020<0607:anolsm>2.0.co;2).
- Collins, W. D., and Coauthors, 2006: The formulation and atmospheric simulation of the Community Atmosphere Model version 3 (CAM3). *J. Clim.*, **19**, 2144–2161,

<https://doi.org/10.1175/JCLI3760.1>.

Coppin, D., and S. Bony, 2015: Physical mechanisms controlling the initiation of convective self-aggregation in a General Circulation Model. *J. Adv. Model. Earth Syst.*, **7**, 2060–2078, <https://doi.org/10.1002/2015MS000571>.

Emanuel, K., A. A. Wing, and E. M. Vincent, 2014: Radiative-convective instability. *J. Adv. Model. Earth Syst.*, **6**, 75–90, <https://doi.org/10.1002/2013MS000270>.

Holloway, C. E., and S. J. Woolnough, 2016: The sensitivity of convective aggregation to diabatic processes in idealized radiative-convective equilibrium simulations. *J. Adv. Model. Earth Syst.*, **8**, 166–195, <https://doi.org/10.1002/2015MS000511>.

Jeevanjee, N., and D. M. Romps, 2013: Convective self-aggregation, cold pools, and domain size. *Geophys. Res. Lett.*, **40**, 994–998, <https://doi.org/10.1002/grl.50204>.

Khairoutdinov, M., and K. Emanuel, 2013: Rotating radiative-convective equilibrium simulated by a cloud-resolving model. *J. Adv. Model. Earth Syst.*, **5**, 816–825, <https://doi.org/10.1002/2013ms000253>.

Khairoutdinov, M. F., and D. A. Randall, 2003: Cloud resolving modeling of the ARM summer 1997 IOP: Model formulation, results, uncertainties, and sensitivities. *J. Atmos. Sci.*, **60**, 607–625, [https://doi.org/10.1175/1520-0469\(2003\)060<0607:CRMOTA>2.0.CO;2](https://doi.org/10.1175/1520-0469(2003)060<0607:CRMOTA>2.0.CO;2).

Kiranmayi, L., and E. D. Maloney, 2011: Intraseasonal moist static energy budget in reanalysis data. *J. Geophys. Res. Atmos.*, **116**, 711–729, <https://doi.org/10.1029/2011JD016031>.

Maloney, E. D., 2009: The moist static energy budget of a composite tropical intraseasonal

- oscillation in a climate model. *J. Clim.*, **22**, 711–729,
<https://doi.org/10.1175/2008JCLI2542.1>.
- Mapes, B. E., 2016: Gregarious convection and radiative feedbacks in idealized worlds. *J. Adv. Model. Earth Syst.*, **8**, 1029–1033, <https://doi.org/10.1002/2016MS000651>.
- Muller, C., and S. Bony, 2015: What favors convective aggregation and why? *Geophys. Res. Lett.*, **42**, 5626–5634, <https://doi.org/10.1002/2015GL064260>.
- Muller, C. J., and I. M. Held, 2012: Detailed investigation of the self-aggregation of convection in cloud-resolving simulations. *J. Atmos. Sci.*, **69**, 2551–2565,
<https://doi.org/10.1175/JAS-D-11-0257.1>.
- , and D. M. Romps, 2018: Acceleration of tropical cyclogenesis by self-aggregation feedbacks. *Proc. Natl. Acad. Sci. U. S. A.*, **115**, 2930–2935,
<https://doi.org/10.1073/pnas.1719967115>.
- Naumann, A. K., B. Stevens, C. Hohenegger, and J. P. Mellado, 2017: A conceptual model of a shallow circulation induced by prescribed low-level radiative cooling. *J. Atmos. Sci.*, **74**, 3129–3144, <https://doi.org/10.1175/JAS-D-17-0030.1>.
- Neelin, J. D., and I. M. Held, 1987: Modeling tropical convergence based on the moist static energy budget. *Mon. Weather Rev.*, **115**, 3–12, [https://doi.org/10.1175/1520-0493\(1987\)115<0003:MTCBOT>2.0.CO;2](https://doi.org/10.1175/1520-0493(1987)115<0003:MTCBOT>2.0.CO;2).
- Nolan, D. S., E. D. Rappin, and K. A. Emanuel, 2007: Tropical cyclogenesis sensitivity to environmental parameters in radiative-convective equilibrium. *Q. J. R. Meteorol. Soc.*, **133**, 2085–2107, <https://doi.org/10.1002/qj.170>.
- Pritchard, M. S., and D. Yang, 2016: Response of the superparameterized Madden-Julian

- oscillation to extreme climate and basic-state variation challenges a moisture mode view. *J. Clim.*, **29**, 4995–5008, <https://doi.org/10.1175/JCLI-D-15-0790.1>.
- Seidel, S. D., and D. Yang, 2020: The lightness of water vapor helps to stabilize tropical climate. *Sci. Adv.*, **6**, eaba1951, <https://doi.org/10.1126/sciadv.aba1951>.
- Sobel, A., S. Wang, and D. Kim, 2014: Moist static energy budget of the MJO during DYNAMO. *J. Atmos. Sci.*, **71**, 4276–4291, <https://doi.org/10.1175/JAS-D-14-0052.1>.
- Sobel, A. H., J. Nilsson, and L. M. Polvani, 2001: The weak temperature gradient approximation and balanced tropical moisture waves. *J. Atmos. Sci.*, **58**, 3650–3665, [https://doi.org/10.1175/1520-0469\(2001\)058<3650:TWTGAA>2.0.CO;2](https://doi.org/10.1175/1520-0469(2001)058<3650:TWTGAA>2.0.CO;2).
- Wing, A. A., and K. A. Emanuel, 2014: Physical mechanisms controlling self-aggregation of convection in idealized numerical modeling simulations. *J. Adv. Model. Earth Syst.*, **6**, 59–74, <https://doi.org/10.1002/2013MS000269>.
- , and T. W. Cronin, 2016: Self-aggregation of convection in long channel geometry. *Q. J. R. Meteorol. Soc.*, **142**, 1–15, <https://doi.org/10.1002/qj.2628>.
- , S. J. Camargo, and A. H. Sobel, 2016: Role of radiative-convective feedbacks in spontaneous tropical cyclogenesis in idealized numerical simulations. *J. Atmos. Sci.*, **73**, 2633–2642, <https://doi.org/10.1175/JAS-D-15-0380.1>.
- Wolding, B. O., and E. D. Maloney, 2015: Objective Diagnostics and the Madden–Julian Oscillation. Part II: Application to Moist Static Energy and Moisture Budgets. *J. Clim.*, **28**, 7786–7808, <https://doi.org/10.1175/JCLI-D-14-00689.1>.
- Yanai, M., S. Esbensen, and J.-H. Chu, 1973: Determination of Bulk Properties of Tropical Cloud Clusters from Large-Scale Heat and Moisture Budgets. *J. Atmos. Sci.*, **30**, 611–

627, [https://doi.org/10.1175/1520-0469\(1973\)030<0611:dobpot>2.0.co;2](https://doi.org/10.1175/1520-0469(1973)030<0611:dobpot>2.0.co;2).

Yang, D., 2018a: Boundary Layer Height and Buoyancy Determine the Horizontal Scale of Convective Self-Aggregation. *J. Atmos. Sci.*, **75**, 469–478, <https://doi.org/10.1175/JAS-D-17-0150.1>.

——, 2018b: Boundary Layer Diabatic Processes, the Virtual Effect, and Convective Self-Aggregation. *J. Adv. Model. Earth Syst.*, **10**, 2163–2176, <https://doi.org/10.1029/2017MS001261>.

——, 2019: Convective Heating Leads to Self-Aggregation by Generating Available Potential Energy. *Geophys. Res. Lett.*, **46**, 10687–10696, <https://doi.org/10.1029/2019GL083805>.

——, and S. D. Seidel, 2020: The Incredible Lightness of Water Vapor. *J. Clim.*, **33**, 2841–2851, <https://doi.org/10.1175/jcli-d-19-0260.1>.

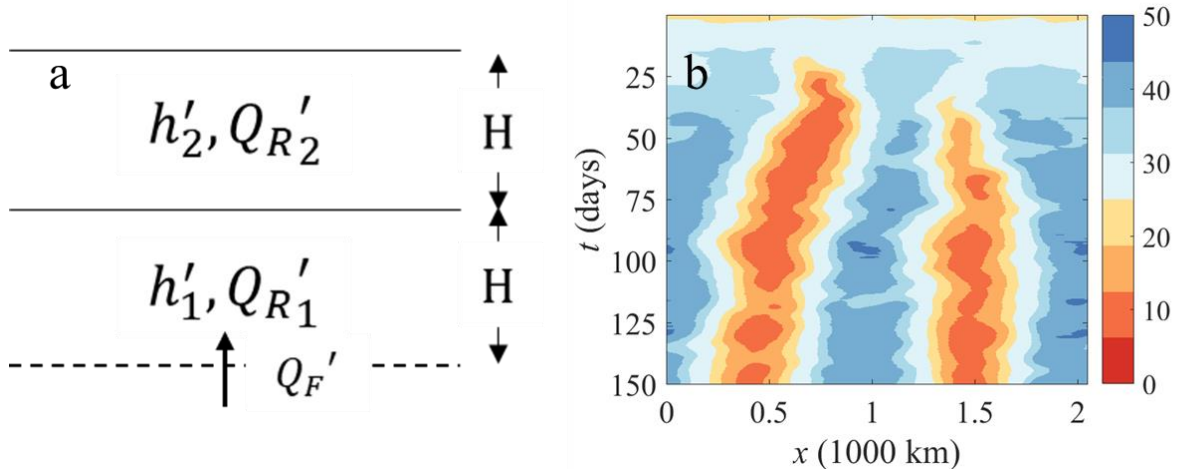


Figure 1. (a) The two-layer schematic of convective self-aggregation. (h', Q_R', Q_F') denote horizontal perturbations of the MSE, radiative cooling rate and surface-flux heating rate, respectively. Their units are all $\text{Jkg}^{-1}\text{s}^{-1}$. The subscripts represent layer numbers. The height for each layer H is constant. (b) Hovmöller diagram of precipitable water (PW, mm) in the control simulation (blue: moist, orange: dry).

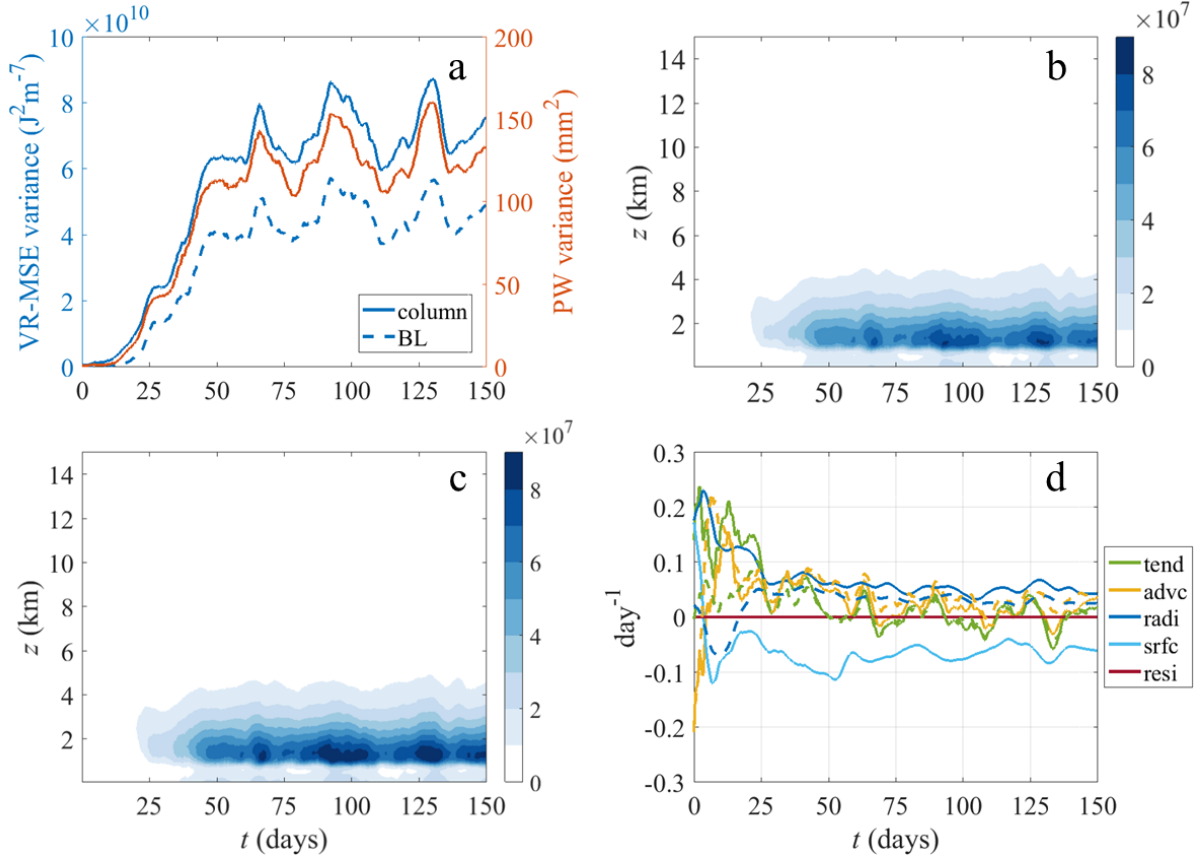


Figure 2. The evolution of VR-MSE variance and its normalized diagnostics in the control simulation. (a) The evolution of VR-MSE variance ($var_R(z)$, blue lines) and PW variance (orange line). The solid blue line denotes the column VR-MSE variance $var_R(z_t)$, and the dashed one denotes the BL variance $var_R(2 \text{ km})$. Panels (b, c) are the vertical distribution of the MSE variance $\overline{(h')^2}$ and the moisture variance $\overline{(L_v q')^2}$ in the troposphere, respectively. The overbar means the horizontal average. (d) Normalized VR-MSE variance diagnosis [see Eq. (16)]. Solid lines represent the whole column integrals ($z = z_t$) while dashed lines represent BL integrals ($z = 2 \text{ km}$). Legend: time derivative of the VR-MSE variance (tend), variance production by advection transport (advc), radiation (radi) and surface fluxes (srfs) and the residual of the VR-MSE budget (resi).

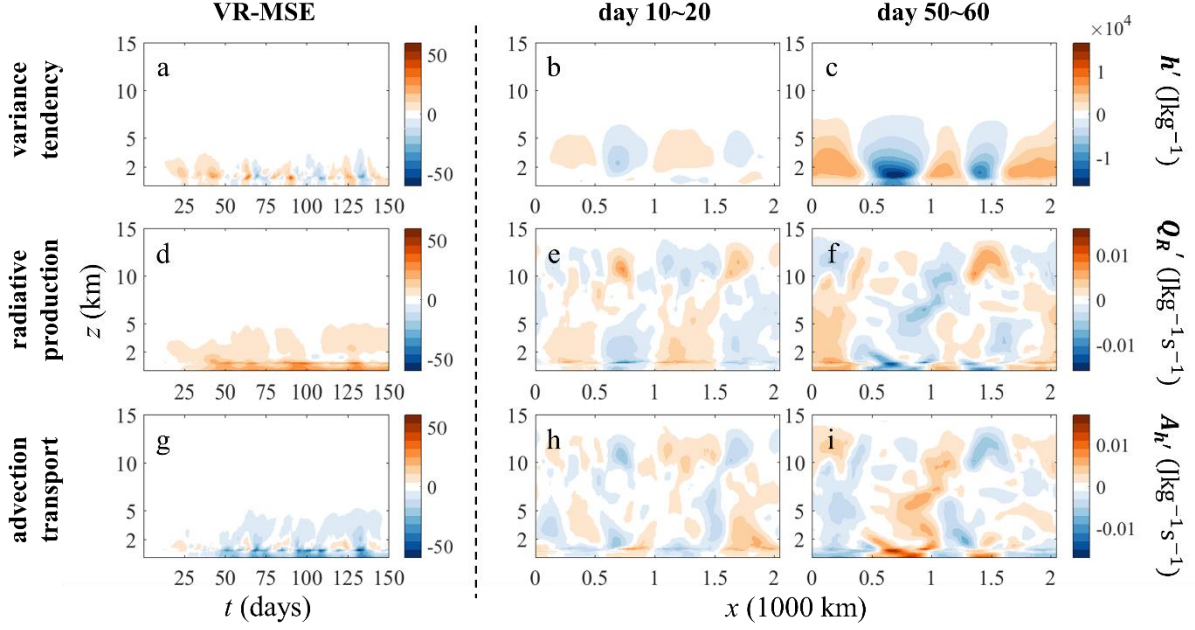


Figure 3. The vertically resolved diagnostics of MSE variance in the control simulation. The left column is the diagnostic results of the local MSE variance budget [see Eq. (14)]. The top to bottom rows are the variance tendency $\partial_t \frac{1}{2} \overline{(\rho_0 h')^2}$, the variance production by radiation $\rho_0^2 \overline{h' Q_R'}$ and the advection transport $-\rho_0^2 \overline{h' \left[\frac{1}{\rho_0} \nabla(\rho_0 \vec{v} h) \right]'}$, respectively. The top to bottom rows in the right two columns are time-averaged MSE anomalies h' , radiative cooling rate anomaly Q_R' and MSE advection $A_{h'} = -\frac{1}{\rho_0} \nabla(\rho_0 \vec{v} h)'$ at two time periods: day 10-20 and day 50-60. The periods correspond to the initiation and development phases of convective self-aggregation, respectively. Near-surface MSE advection is excluded here.

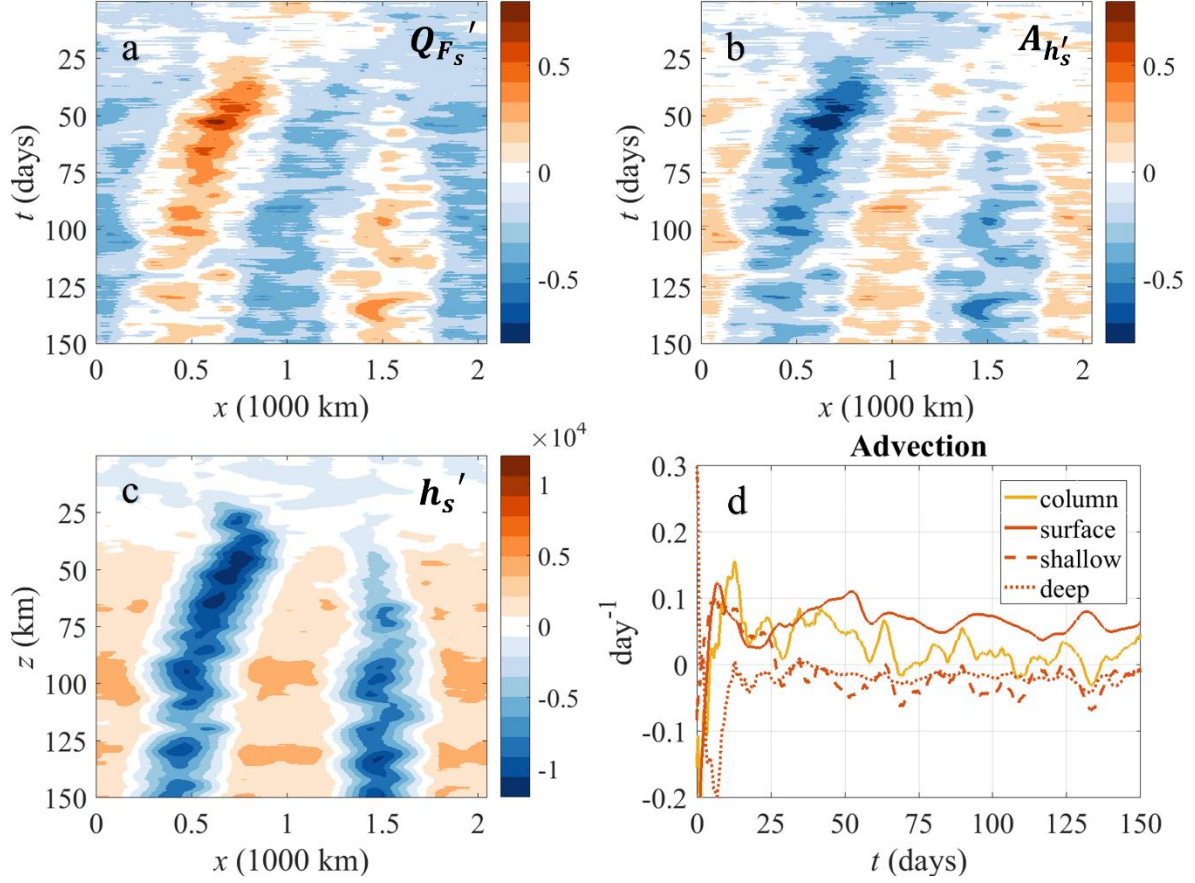


Figure 4. Hovmöller diagrams of (a) heating by surface fluxes (Q_{F_s}' , unit: $\text{Jkg}^{-1}\text{s}^{-1}$), (b) near-surface MSE advection ($A_{h_s}' = -\frac{1}{\rho_0}\nabla(\rho_0\vec{v}h)'|_{z_0}$, unit: $\text{Jkg}^{-1}\text{s}^{-1}$) and (c) near-surface MSE anomalies (h_s' , unit: Jkg^{-1}). (d) The normalized variance production by advection [see Eq. (16)]. Shallow advection refers to advection in the BL (except for the near-surface level), and deep advection refers to that above the BL. Column advection equals to the sum of all.

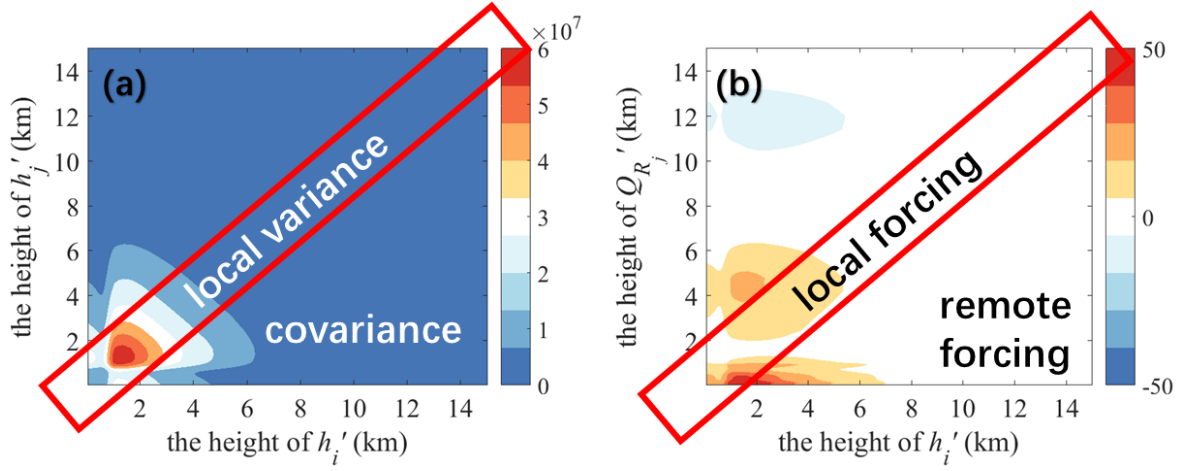


Figure A1. The VI-MSE variance [Eq. (10)] and its production due to radiative cooling [Eq. (11)] in the control simulation. Panels (a, b) are matrices of $h'_i \cdot h'_j$ and $Q_{Rj}' \cdot h'_i$ at the stable state, respectively (averaged over the last 30 days and in x direction). Here, subscripts i and j represent vertical levels. The local variance in Eq. (10) and the local forcing in Eq. (11) correspond to the local components in the red boxes, where $i = j$. Similarly, the covariance in Eq. (10) and the remote forcing in Eq. (11) correspond to the remote components outside the red boxes, where $i \neq j$.